Correlating Local Morphology and Charge Dynamics via Kelvin Probe Force Microscopy to Explain Photoelectrode Performance

Maryam Pourmahdavi,[1,2] Mauricio Schieda,[1] Ragle Raudsepp,[1] Steffen Fengler,[1] Jiri Kollmann,[1] Yvonne Pieper,[1] Thomas Dittrich,[3] Thomas Klassen,[2,4] and Francesca M. Toma[1,2,5,*]

[1] *Institute of Functional Materials for Sustainability, Helmholtz-Zentrum Hereon, Teltow, Germany*
[2] *Faculty of Mechanical and Civil Engineering, Helmut Schmidt University, Hamburg, Germany*
[3] *Nanoscale Solid-Liquid Interfaces, Helmholtz-Zentrum Berlin für Materialien und Energie, Berlin, Germany*
[4] *Institute of Hydrogen Technology, Helmholtz-Zentrum Hereon, Geesthacht, Germany*
[5] *Chemical Sciences Division, Lawrence Berkeley National Laboratory, Berkeley, USA*

(Received 16 August 2024; accepted 15 April 2025; published 9 June 2025)

Photoelectrochemical (PEC) cells have emerged as a promising and sustainable route for the production of valuable chemicals and have attracted significant attention over the last few decades. However, photoelectrodes, essential components of PEC devices, are limited by solar-to-hydrogen conversion efficiencies significantly below the theoretical values, as well as by low stability under working conditions. An important hurdle toward achieving high efficiency is the limited number of available tools that can directly probe the interplay between the local morphology and charge carrier transport dynamics within the photoelectrode top layer. This layer has different functions: providing photocatalytic active sites and protecting underlying layers. Therefore, the development of a powerful technique to reveal the influence of morphology on transport dynamics is crucial. In this work, we show how to precisely correlate local morphology with optoelectronic properties via the investigation of photoinduced charge transport processes, by time-dependent Kelvin probe force microscopy (KPFM) measurements. Our approach allows the extraction of time-dependent photovoltage for each pixel of a KPFM scan. We used crystalline-amorphous mixed phase TiO_2 as a well-established model system to apply and validate our method. Through local correlations between structure-morphology and optoelectronic properties, our results reveal more efficient photoinduced charge separation on the regions corresponding to the crystalline TiO_2 phase, which exhibit faster transport, and generate a significantly higher surface photovoltage signal (approximately 440 mV) upon UV illumination (super-band-gap illumination). This finding supports the considerable role of microstructure in charge carrier dynamics, and the ability of our analytical method to resolve it. The analysis technique outlined here should find broad applicability, enabling in-depth insight into the effect of local microstructure, and contributing to the design and development of more efficient photoelectrodes by tailoring of the microstructure at the nanoscale.

DOI: 10.1103/PRXEnergy.4.023010

I. INTRODUCTION

Photoelectrochemical (PEC) cells are devices that harness solar energy and directly use it to drive chemical reactions, such as splitting water into hydrogen and oxygen [1–3] or converting CO_2 into valuable chemicals [4,5]. In these devices, semiconductor materials absorb sunlight, generating electron-hole pairs that drive oxidation and reduction reactions at electrode/electrolyte interfaces [6–8]. However, challenges such as the limited efficiency and stability of current materials present hurdles for commercialization of these technologies [9,10]. Therefore, a large fraction of the research efforts is focused on developing efficient photoelectrodes, increasing stability, and reducing costs [11–14] to make PEC cells viable and scalable solutions for sustainable fuel production, paving the way for a future with clean energy. Despite extensive research on designing macroscopically efficient photoelectrodes, there is limited information available to answer the question of how the microstructure influences charge

*Contact author: francesca.toma@hereon.de

Published by the American Physical Society under the terms of the Creative Commons Attribution 4.0 International license. Further distribution of this work must maintain attribution to the author(s) and the published article's title, journal citation, and DOI.

carrier transport within the conductive protective photoelectrode top layer, where the separated charges need to reach the electrolyte interface and drive photoelectrochemical reactions. This is due to the limited number of available powerful methods to investigate and resolve the interplay between the microstructure and charge carrier transport dynamics down to the nanoscale. Therefore, it is vital to develop effective techniques to enable researchers to precisely investigate intrinsic light-induced properties and particularly the role of microstructure in charge carrier transport, which considerably affects the macroscopic performance of the device.

Kelvin probe force microscopy (KPFM) is a scanning probe method that enables the measurement of local surface potential with spatial resolution down to the nanoscale. When combined with illumination, KPFM allows nanoscale photovoltage measurements. For instance, Fuchs *et al*. [15] have acquired maps of regions of interest on organic photovoltaic blends, both in the dark and under illumination. By taking the difference between these maps, they generated surface photovoltage (SPV) maps. Other studies have demonstrated the use of KPFM with modulated illumination to capture either the transient behavior or the spectral response at a single point of interest on the sample surface[16–18]. To measure transient behavior across an entire region of interest (ROI), each point must typically be measured one after another. Alternatively, by repetitively scanning the ROI, one can generate transients for each point, with a sampling rate determined by the frame rate of the mapping. In the first approach, accurately estimating time constants at any point of interest requires that the signal be tracked until it has completely decayed. Otherwise, fast-decaying components may dominate the signal, while slower components may be missed entirely (for a discussion of fast and slow SPV states, see Ref. [19]). As a result, this method is generally limited to measuring short time constants.

In contrast, repetitive mapping of the entire ROI requires only that a series of maps be acquired until the signal has decayed once. A variation of this approach was presented by Escasain *et al*. [20], where each scan is performed successively with and without illumination. However, this method is limited to samples with time constants short enough to allow the SPV signal to fully decay between the first scan and the second scan. If it does not, only part of the signal is captured, and the increasing off-time during the second scan can lead to an apparent rise in the SPV signal within a single scan line.

To increase the sampling rate, Checa *et al*. [21] proposed sparse scanning KPFM, which achieves frame rates of several frames per second by scanning the area of interest with reduced measurement point density, followed by image reconstruction using Gaussian processing. While this method significantly increases the measurement speed, it also reduces the spatial resolution and introduces artifacts that are independent of the number of cycles. This limits its effectiveness, especially when the dynamic phenomena of interest occur at length scales close to the instrument's resolution limit.

In this work, we present a method that can be implemented with any standard KPFM system, without the need for additional hardware. It takes advantage of the fact that any ROI defined by the same physical properties must exhibit the same transient behavior. This characteristic allows a sampling rate not in the second range, but in the millisecond range.

We developed this analytical method to gain in-depth insight into the dependency of charge carrier dynamics on microstructure, obtained by KPFM and Kelvin probe (KP) methods. We used TiO_2 as a useful model system to apply and validate the effectiveness of our method. TiO_2 has attracted significant attention due to its favorable properties, such as high chemical stability, low cost, and excellent photoactivity [22–25]. The top layer of photoelectrodes is usually covered by a TiO_2 thin film grown by atomic layer deposition (ALD) to protect underlying layers from corrosion under harsh PEC conditions [26–28]. However, this layer should also act as an efficient charge transport layer to facilitate the driving of electrochemical reactions at the surface [29]. Therefore, this material is a useful platform for our intended investigations on the microstructure, since microstructure plays a critical role in affecting charge transport within semiconductor materials by factors such as crystallinity [30], grain and facet boundaries [31], and defects [32]. These parameters considerably affect the diffusion and recombination rates of charge carriers. Consequently, tailoring the microstructure of photoelectrodes is a strategic approach to enhance charge carrier transport and, eventually, increase the overall efficiency of PEC devices.

We used the KP method and KPFM to obtain the required charge carrier dynamics data. The KP method is widely used to measure surface photovoltage, which is an indication of charge carrier separation efficiency. It operates by nullifying the light-induced change of the potential difference between the sample and the reference electrode with an external voltage [33]. KP measurements provide valuable information about the charge carrier dynamics, including separation, transport, and recombination of charge carriers [29]. KPFM complements the KP method by providing nanoscale insight into the local electronic properties of surfaces. This technique allows the mapping of surface potential variations with high spatial resolution, enabling the correlation of microstructural features with charge transport behavior [34]. The combination of the KP method and KFFM offers a powerful method to investigate charge carrier dynamics in photoelectrodes. X-ray diffraction was used to confirm the nature of microstructural features in the analyzed samples.

Here we demonstrate how we can gain information about charge carrier dynamics in mixed-phase (crystalline-amorphous) TiO_2 samples by following the light-driven evolution of the surface potential by KPFM maps. Our method can precisely extract the full temporal resolution available in the KPFM results and reveal a more effective charge carrier separation through the regions corresponding to crystalline TiO_2, which not only showcases the significant effect of microstructure on the optoelectronic properties but also demonstrates the effectiveness of our method to resolve these underlying phenomena at the nanoscale.

While TiO_2 represents a model system to test the feasibility of our approach, the method developed in this work can be directly implemented for other promising material systems and thus provides a useful tool for researchers working on understanding and developing more-efficient and more-sustainable energy conversion systems.

II. RESULTS AND DISCUSSION

A. Microstructure characterization

Thermal ALD (see Sec. IV) was used to obtain a series of TiO_2 coatings at increasing synthesis temperatures. As evidenced by Raman spectroscopy and x-ray diffraction (Fig. S1 in Supplemental Material [44]), the films synthesized at 180 °C are fully amorphous. As the temperature increases, crystalline inclusions of anatase TiO_2 grow within the amorphous phase, and beyond 260 °C the films are fully crystalline. The sample synthesized at 220 °C was chosen as a model system for analysis in this work. This sample features a mixed-phase structure, including crystalline TiO_2 (anatase, see Fig. S1 in Supplemental Material [44]), embedded within an amorphous TiO_2 matrix. This observation is supported by the topography images obtained by atomic force microscopy (AFM) shown in Figs. 1(a) and 1(b). This morphology is especially useful as a model system because of the presence of both crystalline and amorphous regions with a width of several hundred nanometers. While AFM is able to finely resolve the crystalline features on the surface of the sample [35], a portion of crystallites remains buried beneath the surface, as evidenced by transmission electron microscopy [TEM; see Figs. 1(c), 1(d), and 1(e)]. We observed similar anatase inclusions in our previous studies on mixed-phase TiO_2 thin films obtained by plasma-enhanced ALD (see Fig. S2 in Supplemental Material [44]) [29]. As the topmost layer of a photoelectrode, this thin film has a dual function. It serves as a protective layer as well as a conductive layer. Under super-band-gap illumination it absorbs light, generates electron-hole pairs, and facilitates the separation of holes toward the surface and electrons toward

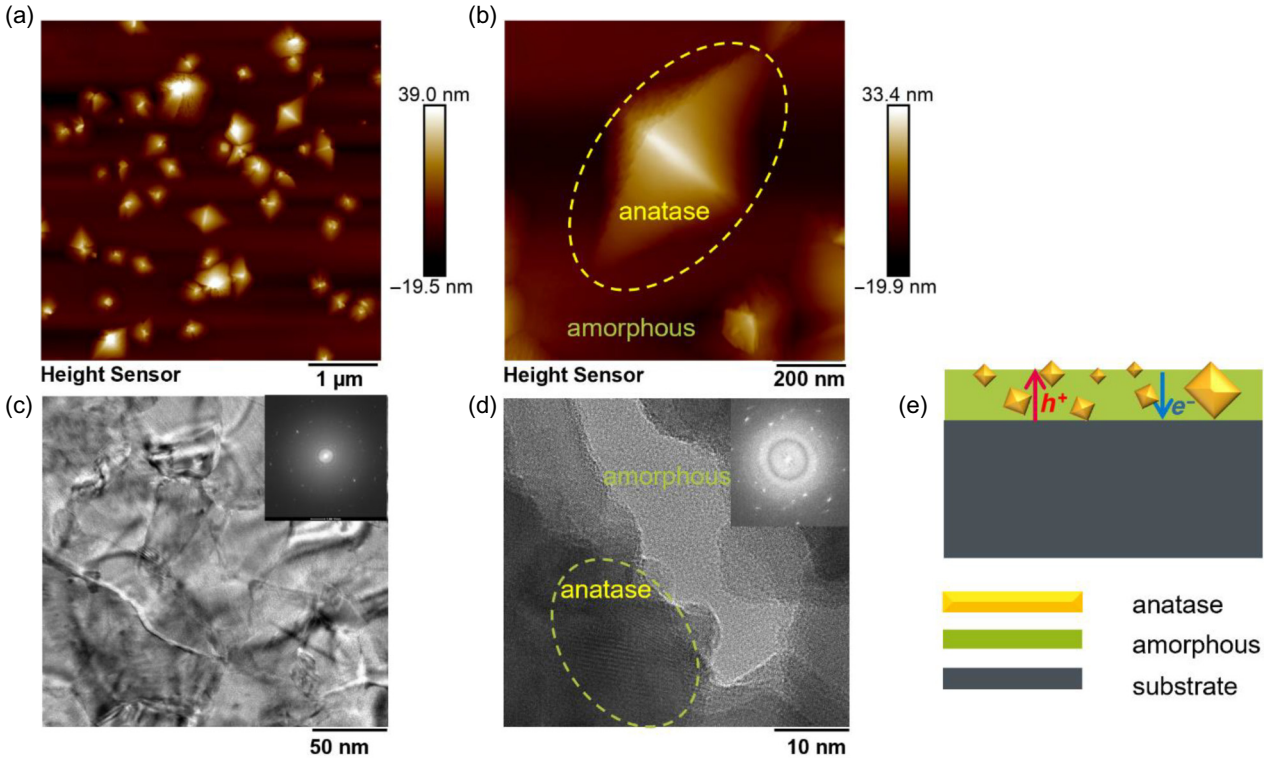

FIG. 1. (a),(b) AFM high-resolution topography of mixed-phase TiO_2 at different magnifications. (c),(d) Surface TEM image of an anatase crystallite embedded in an amorphous matrix. (e) Cross-section schematic of charge transport across the microstructure of the deposited film.

the back contact. Charge separation in these layers is facilitated by the space charge region at the surface and by the heterojunction at the contact with the Si substrate [36]. This effect contributes to driving electrochemical reactions, such as water oxidation, at the electrode/electrolyte interface, as schematically illustrated in Fig. 1(d).

The microstructure substantially influences charge carrier transport within the layer, significantly affecting the macroscopic photoelectrochemical performance of the device. To understand the processes involved in the charge carrier transport at both the macroscopic and the microscopic scales, KP measurements and KPFM can be used as complementary techniques, with KP measurements allowing a higher signal-to-noise ratio and KPFM providing high spatial resolution.

B. Measurements of charge carrier dynamics

1. KP measurements

Surface photovoltage analysis by KP measurements is an established method to study overall charge carrier dynamics over the entire sample. Particularly, it gives insights into fast and slow charge carrier dynamic processes within the bulk of materials over long periods [33]. To analyze the photoinduced charge separation, we performed contact potential difference (CPD) measurements on TiO_2 model samples with and without illumination. The different contributions to the SPV signal originating from distinct charge carrier transport processes were obtained by our fitting the experimental data with a sum of exponential functions. The fit was performed separately for the different measurement phases in both dark and illuminated conditions with two and three exponential functions, respectively (see Sec. II A in Supplemental Material [44] for further details). Fast processes are characterized by a steep slope, and slow processes are characterized by a gentle slope. Detailed extracted amplitudes and time constants related to these processes are reported in Table I. During the illumination (excitation) phase, fast processes occur with characteristic times within the 10 s range, while slow processes show characteristic times of hundreds of seconds (344–371 s). With light OFF during the relaxation phase, fast processes occur with characteristic times in the tens of seconds range (26–29 s), whereas slow processes occur with characteristic times on the order of hundreds of seconds (334–423 s).

By studying electrodes prepared with TiO_2 nanoparticles, Henning *et al.* [34] observed similarly long (seconds to minutes) overall relaxation times. They attributed these values to the high relative permittivity of TiO_2, which acts as the dielectric in a capacitor. They fitted their experimental data with the sum of two exponential functions, corresponding to a slow component and a fast component. The slow component was attributed to electron diffusion across the TiO_2 network toward the back contact, a slow process due to trapping and detrapping in surface and bulk defect states. The fast component was attributed to recombination processes within single particles.

To resolve and distinguish these fast and slow processes on our model system, and assign them to different regions of the samples, a technique with high spatial resolution is required. This information can be provided by KPFM, a powerful complementary technique that correlates topographic features with underlying local charge carrier dynamics with nanoscale resolution.

2. KPFM measurements

For KPFM measurements, a region of the sample was scanned continuously in the initial dark conditions for 60 min, followed by scanning under illumination for 70 min and finally in the dark for 80 min, to follow the evolution of the surface potential over time.

The result is a series of consecutive surface potential maps. By one defining regions of interest, surface potential transients can be extracted for specific locations on the surface of the sample.

Two methods were used for the analysis of the experimental data: the “manual” method is straightforward, but requires averaging over regions of space and time, and hence does not use the full resolution of the measurement; the “automated” method allows full utilization of the information contained for each pixel within the KPFM maps.

The following sections describe the implementation of each of these methods. Further details are given in Sec. II B in Supplemental Material [44].

TABLE I. Amplitude A and time t characteristics of fast, slow, and intermediate processes extracted from the SPV signal. The error values reported correspond to the precision of the fitting. The fit describes the average CPD curve for a given ROI [see Fig. 2(a)].

Phase	A_f (mV)	A_s (mV)	A_i (mV)	t_f (s)	t_s (s)	t_i (s)	$U_{CPD,0}$ (mV)
Initial	-15 ± 0.09	-126 ± 0.09		682 ± 42	4314 ± 142		-51.34 ± 0.05
ON 1	238 ± 0.3	-135 ± 0.4	53 ± 0.4	93.6 ± 0.3	3339 ± 266	884 ± 65	141.2 ± 0.3
OFF 1	-78 ± 0.2	-178 ± 0.2		256 ± 1	3341 ± 14		-75.3 ± 0.3
ON 2	188 ± 0.6	-78 ± 0.5	32 ± 0.5	91.8 ± 0.4	3706 ± 132	465 ± 17	99 ± 2
OFF 2	0.15 ± 0.005	-108 ± 0.4		286 ± 2	4227 ± 18		-116.0 ± 0.4

3. Manual analysis of consecutive KPFM maps

KPFM enables imaging of the CPD between the AFM probe and the sample, and simultaneous acquisition of the corresponding topography [Figs. 2(a) and 2(b)]. Consecutive measurements in both dark and illuminated conditions enable nanoscale determination of the light-induced CPD shift (ΔU_{CPD}). The shift in contact potential difference induced by illumination is of the same value, but opposite sign, as the surface photovoltage: $U_{\mathrm{SPV}} = -\Delta U_{\mathrm{CPD}} = -(\mathrm{CPD}_{\mathrm{light}} - \mathrm{CPD}_{\mathrm{dark}})$. Such measurements provide information on the spatial separation of charge carriers, which is limited also by electron-hole pair recombination and which can therefore indicate enhanced photocatalytic activity [37]. To analyze our data, we identified regions of interest that showed the presence of crystalline and amorphous features [Figs. 2(b) and 2(c)]. We performed a series of 23 time-dependent KPFM measurements (m1–m23) in the dark and under illumination. On the representative potential map under the initial dark condition [m7, in Fig. 2(b)], regions corresponding to the crystallites look more blueish than the amorphous matrix, indicating that crystallites have initially more positive CPD than the amorphous component. The average CPD for the whole potential map is approximately −236 mV, as seen from the corresponding data histogram. Upon illumination (m8), the surface potential shifts significantly toward more negative values and crystalline regions look more reddish than the amorphous matrix, evidencing a more negative surface potential on these areas. Under illumination (m8), several peaks appear in the data histogram, which can be attributed to different regions of the sample shifting at different rates toward negative values. The fastest-changing peak (on the left) has its maximum at around −656 mV, highlighting a high negative CPD shift corresponding to high positive surface photovoltage ($U_{\mathrm{SPV}} = -\Delta U_{\mathrm{CPD}}$). This is assigned to mostly crystalline regions, where defect density is lower and mobility higher. The slowest-changing peak (on the right) is assigned to mostly amorphous areas, with higher defect density and correspondingly lower mobility, showing an average CPD of −261 mV, and generating a small SPV amplitude. A negative CPD shift under illumination (positive SPV signal) is an indication of separation of holes toward the surface, or of electrons toward the back contact, or both these processes concomitantly [38]. Under super-band-gap illumination, a separation of holes toward the surface is evidence of the *n*-type behavior of TiO_2. The amplitude (magnitude) of the CPD shift (equal to the magnitude of the photovoltage, since $|\Delta U_{\mathrm{CPD}}| = |U_{\mathrm{SPV}}|$) is a measure of the charge carrier separation efficiency [39]. In *n*-type TiO_2, electron-hole pairs can be generated under illumination with ultraviolet light wavelengths. Majority charge carriers are trapped in surface states, leading to band bending, and consequently to a reduced density of majority charge carriers in the vicinity of the surface in comparison with the bulk value, and resulting in a space charge region (SCR). This is also called a "depletion region" due to the reduced density of majority charge carriers in comparison with the density of fixed charge due to ionized dopants. For *n*-type semiconductors, electrons are captured by surface states and an upward band

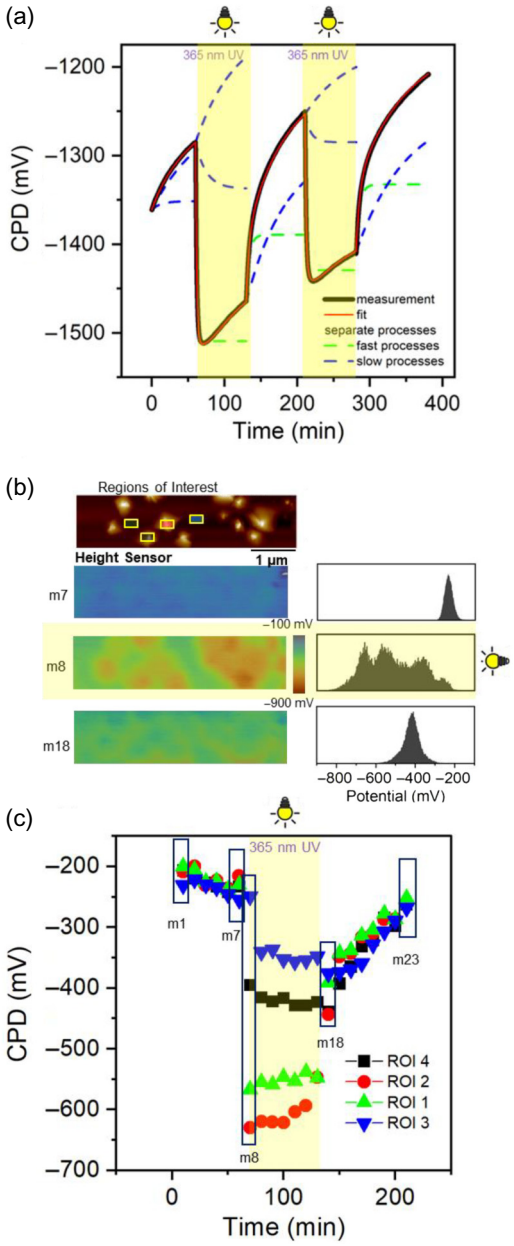

FIG. 2. (a) CPD transients of TiO_2 obtained by Kelvin probe measurements in the dark and under illumination, showing fast and slow processes contributing to the CPD signal. (b),(c) Analysis of consecutive KPFM measurements obtained in the dark and under illumination, and manual analysis of the time dependence of the potential. (b) Manually defined regions of interest based on topography, and examples of potential maps before, during, and after illumination. (c) Extracted CPD transients for each manually defined ROI over time. m, KPFM measurement (potential map).

bending occurs, in conjunction with the formation of a built-in electric field over the SCR, with direction from the bulk to the surface, due to the net negative charge at the surface and net positive charge in the SCR. Upon illumination, photogenerated electron-hole pairs are separated by the charge density gradient in the SCR. In the SCR of an *n*-type semiconductor, photogenerated electrons and holes are transported toward the bulk and the surface, respectively, and therefore the net surface charges are reduced. In other words, the surface potential barrier or surface upward band bending is reduced and the surface potential increases. The change of the surface potential results in a positive SPV signal (negative CPD shift) [36]. The SPV corresponds to the reduction in band bending, the energetic difference between quasi-Fermi-levels of electrons and holes (E_{Fn} and E_{Fp}) [40]. Due to the higher local and longer-range order in more-crystalline regions, scattering is minimized, resulting in fast carrier transport processes and the generation of SPV (ΔU_{CPD}) signals of higher amplitude. This translates into higher charge carrier separation efficiency, in agreement with previous studies [41,42].

To follow the evolution of surface potential over time, based on a series of measurements (m1–m23) performed in the dark and under illumination, the time dependencies of the SPV signals of different manually defined regions of interest (ROI 1, ROI 2, ROI 3 and ROI 4) were reconstructed [Fig. 1(b)]. Regions corresponding to crystalline phase (ROI 1 and ROI 2) generate a fast negative CPD shift with a steep slope and high SPV amplitude compared with the amorphous regions (ROI 3 and ROI 4), which exhibit a slow process (gradual slope) and low SPV amplitude. A positive SPV signal can also be viewed as resulting from accumulation of holes [43]. The entire surface generates positive SPV signals with different signal amplitudes. Therefore, crystalline surfaces accumulate higher densities of photogenerated holes in comparison to amorphous regions. Hence, crystalline areas offer higher densities of holes for driving oxidation reactions at the surface.

Note that since crystallites are embedded in an amorphous matrix, the observed SPV transients may also contain a partial contribution from diffusion of charge carriers, driven by charge density gradients at the homojunctions (phase junctions) between the walls of the crystalline inclusions and surrounding amorphous TiO_2 regions. While we observe charge trapping at the phase junction interface, we do not observe increased charge separation. The highest potential shift is observed within the crystallites, and not at the boundaries with the amorphous regions. There is no indication that band alignment at this junction is beneficial. This point is discussed further in the next section.

The study of mixed-phase samples in successive dark and illumination conditions showcases the power of KPFM to correlate topography with surface potential, and to investigate the charge carrier dynamics with high spatial resolution.

4. Automated analysis of consecutive KPFM maps

To optimize the manual analysis and more precisely correlate surface potential with the topography, a robust technique was developed in this study. The following is a description of the method (additional details are provided in Sec. II B 2 in Supplemental Material [44]).

A surface potential map, obtained during the last measurement under continuous illumination and after the steady state had been reached, was used as a reference to generate several regions of interest [Fig. 3(a)].

The histogram for this reference image is used to define the "masks": that is, the sets of pixels that will be analyzed for each ROI. On the basis of the data histogram [Fig. 3(b)] extracted from the reference image in Fig. 4(a), we identified eight peaks. The CPD range in which a given peak in the histogram is dominant (see Supplemental Material [44]) determines the pixels on the CPD map that constitute the mask assigned to that peak, defining the ROI of that peak. Note that, in this way, regions of interest are defined as ranges on the data histogram for the reference surface potential map. The actual pixels corresponding to that ROI (its mask) are fixed for the rest of the analysis by their value on the reference map and not by their coordinates, as would be the case in the "manual" method described in the previous section.

Figure 3(c) shows overlays of the reference surface potential map on the topography map, with masks corresponding to different regions of interest. By analyzing the identified regions of interest in all images in the series [Fig. 3(c)], we extracted the surface potential for each pixel of each ROI. Subsequently, we plotted each CPD value as a function of the acquisition time for that pixel. This is possible because a time stamp can be obtained for the CPD values for each pixel, of each ROI, in each map. The result gives information about the evolution of the surface potential for the identified regions of interest, taking advantage of the time resolution given by the sampling rate of the KPFM measurement and stored in the potential map data [Fig. 3(d)].

In this way, we can derive the changes in CPD of different regions of the samples in the dark and under illumination. Starting from a steady-state CPD value in the dark that is similar for all the regions of interest, illumination generates CPD transients with different length amplitude and slope steepness, depending on the ROI under examination. Subsequently, when light is turned off, a second transient with a different slope is formed with a CPD value similar for all the regions of interest.

For the model system investigated here, on the basis of the magnitude and the slope of the photovoltage (ΔU_{CPD}

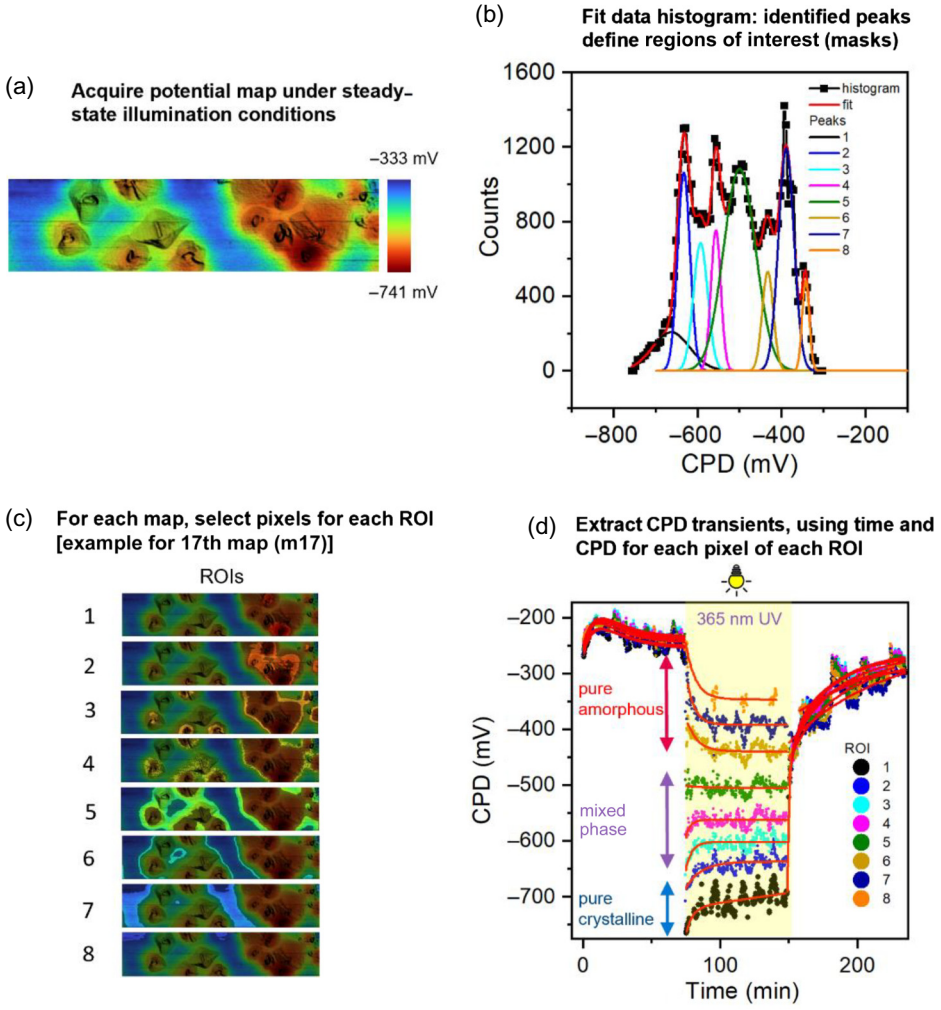

FIG. 3. Extraction of photovoltage transients from consecutive potential maps by the automated method (see the text for details), with the use of the full temporal resolution provided by the KPFM measurements. The fluctuations [(d)] are not related to measurement sensitivity, but instead correspond to the potential range under each peak in the histograms identified in (a) for the definition of the regions of interest (see the text for details).

shift) transients extracted, three main categories of surface regions may be identified: mostly amorphous (ROI 6, ROI 7, and ROI 8), mixed crystalline and amorphous (amorphous layer covering a hidden portion of crystallites underneath; ROI 3,ROI 4, and ROI 5), and mostly crystalline (ROI 1 and ROI 2).

Figure 4 shows schematic band diagrams for the crystalline and amorphous TiO_2 phases in conditions with and without illumination, as well as a schematic cross section of the mixed-phase TiO_2 thin films. Under illumination, predominantly amorphous regions exhibit slower charge carrier separation and a low SPV (ΔU_{CPD} shift) amplitude in comparison with the crystalline regions. This behavior is attributed to higher defect densities in the disordered structure of the amorphous phase [41] leading to charge trapping and increased recombination in comparison with the crystalline phase. Regions of mixed phase show intermediate relaxation times to reach the steady state, and moderate SPV signal amplitudes. An example of this is locations within the crystallite but at a distance less than the minority carrier diffusion length, in the immediate vicinity of the amorphous crystalline homojunction. Regions corresponding to mostly crystalline phase show the fastest process with the highest resolved SPV (ΔU_{CPD} shift) amplitude (approximately 440 mV). This behavior is attributed to the ordered structure of crystallites [41], which facilitates faster charge carrier transport. Thus, because of the higher and longer-range order of the crystalline regions compared with the amorphous material, the closer to the crystallites, the faster the processes, and the further away from the crystallites, the slower the processes.

A more detailed examination of the photovoltage transients reveals additional complexity. For instance, in ROI 8, the CPD follows a simple exponential decay. In contrast, ROI 1 exhibits a more complex behavior, with recovery that includes a fast decay and an additional slower signal contribution with an opposite trend, indicating an opposite direction of charge separation. This behavior is attributed to the movement of electrons toward electron-trap states at the crystallite surfaces. It is worth noting that this process might also occur in the amorphous regions. However, the similarity of time constants makes it challenging to analytically distinguish it from the slow hole diffusion process. Regarding the phase junction

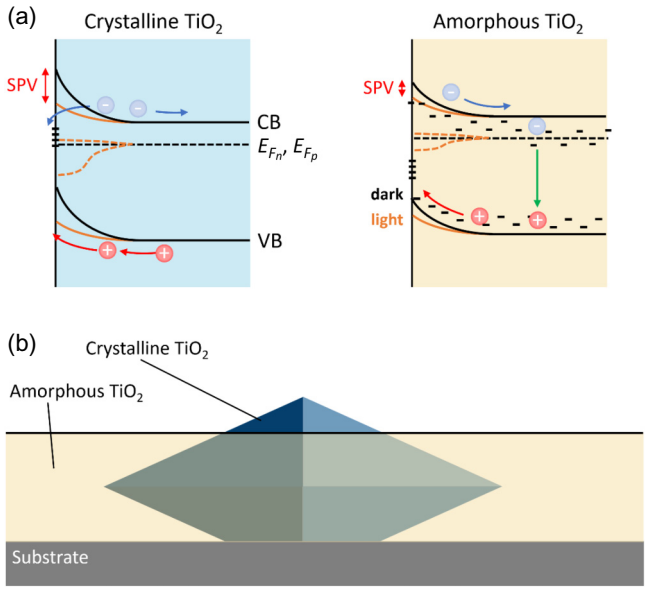

FIG. 4. (a) Schematic band diagrams for crystalline and amorphous regions of TiO_2, in dark conditions and under illumination. (b) Cross-section schematic model of a TiO_2 crystallite embedded in an amorphous TiO_2 matrix. See the text and Supplemental Material [44] for additional details. CB, conduction band; VB, valence band.

between the walls of the crystalline inclusions and the surrounding amorphous TiO_2 regions, as discussed in the previous section, we do not observe increased lateral charge separation. If electrons and holes were separated at the junction, with electrons moving toward the crystalline phase and holes toward the amorphous phase, we would expect a different distribution of charge density. Specifically, the density of trapped holes in the amorphous phase near the junction would decrease, leading to a smaller light-induced change in the CPD compared with that in amorphous regions farther from the junction. Conversely, in the crystalline phase near the junction, the light-induced CPD change would increase relative to that in crystalline regions farther away. However, our measurements contradict this expectation. The amorphous and crystalline phases closest to the junction exhibit, respectively, the strongest and the weakest light-induced CPD changes within their respective phases. This might misleadingly suggest that electrons and holes are instead separated toward the crystalline and amorphous phases, respectively. However, the positive signal component in the transients associated with the crystalline phase under illumination remains consistent, regardless of the distance from the phase junction. This consistency indicates that electron traps at the crystalline surface are the dominant contributors to the signal. This observation also explains the increased light-induced CPD change in the amorphous phase surrounding an exposed crystallite. It is reasonable to assume that additional crystalline material lies buried beneath the amorphous layer, trapping electrons from the adjacent amorphous phase. It is important to note that the TiO_2 layer thickness is only about 1% of the width of the measured maps, which must be considered when one is interpreting these results.

While these findings suggest that surface trapping and band bending dominate the observed behavior, they do not entirely exclude the possibility of beneficial charge alignment at the phase junction interface. Since our measurements capture the surface potential, all we can conclude is that surface-level trapping and band bending are the primary phenomena at play. Further semiquantitative observations of the photovoltage transients obtained can be used to obtain more detailed but preliminary interpretations, to be verified by complementary analysis. These are summarized in Supplemental Material [44].

Microstructure has a profound influence on the dynamics of charge carriers, and the mostly crystalline phase exhibits more efficient charge carrier separation and ultimately enhanced macroscopic photoelectrochemical performance. The method for KPFM data masking and pixel tracking demonstrated here enables a full use of the time resolution available within potential maps, enabling a more detailed analysis of photovoltage evolution at the nanoscale.

III. CONCLUSION

In this work, we have outlined an analysis method to extract the full temporal resolution available in the KPFM maps. For the model samples studied here, our findings showcased the higher efficiency of photoinduced charge separation on the mostly crystalline TiO_2 phase, marked by a rapid and considerably high surface photovoltage signal (approximately 440 mV) upon UV illumination. Conversely, regions corresponding to the mixed phase and mostly amorphous material exhibited intermediate and slow processes with low SPV amplitude, respectively, due to disordered microstructure and higher defect density of the amorphous phase, which serve as charge carrier recombination centers. This approach to follow the evolution of surface potentials, within different regions of the sample over time, facilitates the extraction of localized CPD transients, revealing the influence of material microstructure on charge transport dynamics across different regions.

The comprehensive analysis technique demonstrated here can provide valuable insights into the correlation between microstructure and surface potential. It constitutes a powerful tool for researchers focused on understanding and developing efficient photoelectrodes through microstructure engineering at the nanoscale.

IV. METHODS

A. Synthesis

TiO_2 thin films were deposited on highly doped *n*-type silicon wafers (5 mΩ cm, Siegert Wafer GmbH) by

thermal atomic layer deposition in an R-200 ALD reactor (Picosun). The films were synthesized at 220 °C, with the use of $TiCl_4$ [electronic grade (99.9999%), Dockweiler Chemicals GmbH] and ultrapure H_2O (resistivity 18.2 mΩ cm) as titanium- and oxygen-containing precursors, respectively. For the synthesis temperature used, 2000 cycles resulted in a film thickness of approximately 70 nm.

B. Characterization

1. AFM topography

AFM measurements were performed with a Bruker Dimension ICON atomic force microscope. High-resolution topography images were obtained in PeakForce Tapping mode with PEAKFORCE-HIRS-SSB probes (Bruker) with nominal tip radius of 1 nm, spring constant of 0.12 N/m, and resonance frequency of 110 kHz. The peak force set point was approximately 1.2 nN. With the PeakForce Tapping mode, the probe-surface contact is very brief, minimizing tip degradation.

2. AFM–photo-KPFM

KPFM measurements were obtained with Bruker's PeakForce KPFM mode. For each scan line, PeakForce Tapping mode was used for acquisition of the topography, and subsequently the probe was lifted (to a lift distance), and frequency-modulated KPFM was used for the potential measurement, with the KPFM bias contact connected the sample.

Highly doped silicon nitride probes (PFQNE-AL, Bruker) with a nominal tip radius of 5 nm, spring constant of 0.8 N/m, and resonance frequency of 300 kHz were used. The peak force set point was approximately 2.2 nN. The lift height during the potential measurements was 50 nm. This value was found on preliminary scans at decreasing lift heights to be a good compromise between noise/artifacts and spatial resolution of the potential measurements for the probe type used and the samples under study. Drive routing was set to "sample" (with this configuration, the CPD of an *n*-type semiconductor shifts to more negative values under illumination). Samples were illuminated with a fiber-coupled light-emitting diode light source (Thorlabs M365FP1) with a nominal wavelength of 365 nm, and the fiber-optic angle of incidence was set to 8°.

The complete measurement series (dark-light-dark) was performed on the same day (with a total duration of 3.5 h), with the same probe. The hard material of the probe and sample, and the use of PeakForce Tapping mode ensure negligible tip degradation. Furthermore, the roughness in the topography map was unchanged between the first measurement and the last measurement, and no morphology changes were observed on the topography scans. Additionally, we observed no abrupt change in the CPD values during the measurement series. These considerations exclude any significant change of the tip by either degradation or contamination with particles.

Our measurements were performed in ambient conditions, with the relative humidity of the room kept at 30%–45%. The humidity sensor, positioned within the AFM enclosure, showed a constant value of around 20%–30% (the AFM enclosure was kept closed for the duration of the experiment).

The potential of the surface can be affected by the presence of a layer of adsorbed water. For absolute work function measurements, operation under ultrahigh vacuum conditions would be necessary [45]. However, even under those conditions the surface potential on TiO_2 has a significant contribution from the surface-induced dipole, arising due to chemical interaction between the tip and the surface [46]. Furthermore, while the work function of the probe can be calibrated by one measuring a reference sample, such as a gold surface, the work function of Au changes by about 0.5 eV over a few weeks of exposure to ambient air [47].

In the method presented here, however, we do not attempt to obtain values of the work function of the sample. Instead, we are interested in the variations in the local potential, as a function of the local sample composition, and, as a result, of the change in the illumination conditions, in order to reveal local carrier dynamics.

Furthermore, nonvacuum conditions have been consistently used in KPFM investigations of photocatalytic and photoactive materials for photoelectrochemistry [31,48,49]. In addition, a recently published review recommends constant ambient relative humidity [50].

Allowing for the presence of a water film better approximates the operating conditions of a material used as a protection layer in a photoelectrochemical cell. For example, using density functional theory simulations, Litke *et al*. [51] showed that for the case of anatase (101) facets, hydrogen bonding with adsorbed water stabilizes surface-trapped holes localized on surface oxygen atoms, lowering hole migration barriers. Under operation, this would increase charge carrier mobility, suppressing electron-hole recombination. Furthermore, through hydrogen bonding this adsorbed layer determines the configuration of water in the vicinity of the surface, directly impacting the water splitting rate [52].

3. Kelvin probe measurements

Kelvin probe measurements were performed in the dark and under illumination with a Kelvin probe S and a Kelvin controller (Besocke Delta PHI GmbH). The measurement regime consisted of an initial 60 min relaxation period in

the dark followed by repeated light ON-OFF cycles consisting of a 70 min illumination phase followed by an 80 min phase without illumination. The illumination of the sample was arranged by our selecting light with a wavelength of 365 nm using a prism monochromator (Zeiss M4 QIII), and a xenon lamp (XBO300) as a light source.

4. KPFM analysis

A series of consecutive KPFM scans was performed on the sample, under conditions changing from dark to under illumination and back to dark.

For a sample area common to all scans in the series, the CPD map from the last scan under illumination was used to define regions of interest on the basis of peaks fitting the histogram of the CPD data. For each pixel within each ROI, the CPD data were extracted from all measurements in the series, and time values for each pixel were assigned with respect to the beginning of the first measurement. The collected data were used to plot surface potential transients for each ROI. See the main text and Supplemental Material [44] for a full description of the method.

5. TEM morphology

The nanostructure of the sample and the phase information were characterized by means of a Talos F200X transmission electron microscope (Thermo Fisher Scientific, Netherlands). The TiO_2 thin film grown by ALD was deposited on a silicon nitride membrane with a thickness of 15 nm and investigated by high-resolution TEM at 200 keV in bright-field mode.

C. X-ray diffraction and Raman spectroscopy

X-ray diffraction was performed in a D8 DISCOVER diffractometer (Bruker) under a grazing incidence angle of 1.0° with a Cu $K\alpha$ source and with the use of a scintillation detector. Raman spectra were obtained with an alpha300 R confocal Raman microscope (WITec) with a laser excitation wavelength of 532 nm at a nominal power of 15 mW. The Raman scattered light was analyzed in a UHTS 300 spectrometer (WITec) with a Peltier-cooled charge-coupled device detector.

ACKNOWLEDGMENTS

The authors acknowledge support from the Helmholtz Association through program-oriented funding (POF IV). F.M.T. acknowledges support from the "Helmholtz Distinguished Professorship" program of the Helmholtz Association. The results are based on work performed by the Clean Energy Manufacturing Program, U.S. Department of Energy, Office of Science, Office of Basic Energy Sciences, Chemical Sciences, Geosciences, and Biosciences Division, under Contract No.DE-AC0205CH11231 (F.M.T. AFM analysis and data interpretation).

DATA AVAILABILITY

The data that support the findings of this article are openly available [53].

[1] R. v. d. Krol and M. Grätzel, *Photoelectrochemical Hydrogen Production* (Springer, New York, 2012).
[2] M. G. Walter, E. L. Warren, J. R. McKone, S. W. Boettcher, Q. Mi, E. A. Santori, and N. S. Lewis, Solar water splitting cells, Chem. Rev. **110**, 6446 (2010).
[3] *Advances in Photoelectrochemical Water Splitting: Theory, Experiment and Systems Analysis* (Royal Society of Chemistry, London, 2018).
[4] V. Kumaravel, J. Bartlett, and S. C. Pillai, Photoelectrochemical conversion of carbon dioxide (CO_2) into fuels and value-added products, ACS Energy Lett. **5**, 486 (2020).
[5] S. Xu and E. A. Carter, Theoretical insights into heterogeneous (photo)electrochemical CO_2 reduction, Chem. Rev. **119**, 6631 (2019).
[6] A. Fujishima and K. Honda, Electrochemical photolysis of water at a semiconductor electrode, Nature **238**, 37 (1972).
[7] H. Song, S. Luo, H. Huang, B. Deng, and J. Ye, Solar-driven hydrogen production: Recent advances, challenges, and future perspectives, ACS Energy Lett. **7**, 1043 (2022).
[8] D. Li, K. Yang, J. Lian, J. Yan, and S. Liu, Powering the world with solar fuels from photoelectrochemical CO_2 reduction: Basic principles and recent advances, Adv. Energy Mater. **12**, 2201070 (2022).
[9] A. Verma and R. G. Pala, Practical semiconductor physics perspective of materials photoelectrochemistry, Curr. Opin. Electrochem. **36**, 101160 (2022).
[10] R. Sathre, J. B. Greenblatt, K. Walczak, I. D. Sharp, J. C. Stevens, J. W. Ager, and F. A. Houle, Opportunities to improve the net energy performance of photoelectrochemical water-splitting technology, Energy Environ. Sci. **9**, 803 (2016).
[11] G. Zeng, T. A. Pham, S. Vanka, G. Liu, C. Song, J. K. Cooper, Z. Mi, T. Ogitsu, and F. M. Toma, Development of a photoelectrochemically self-improving Si/GaN photocathode for efficient and durable H_2 production, Nat. Mater. **20**, 1130 (2021).
[12] S. Vanka, G. Zeng, T. G. Deutsch, F. M. Toma, and Z. Mi, Long-term stability metrics of photoelectrochemical water splitting, Front. Energy Res. **10**, 840140 (2022).
[13] W. Yang, R. R. Prabhakar, J. Tan, S. D. Tilley, and J. Moon, Strategies for enhancing the photocurrent, photovoltage, and stability of photoelectrodes for photoelectrochemical water splitting, Chem. Soc. Rev. **48**, 4979 (2019).
[14] Tobias A. Kistler, Guosong Zeng, James L. Young, Lien-Chun Weng, Chase Aldridge, Keenan Wyatt, Myles A. Steiner, Oscar Solorzano Jr., Frances A. Houle, Francesca M. Toma, Adam Z. Weber, Todd G. Deutsch, and Nemanja Danilovic, Emergent degradation phenomena demonstrated

on resilient, flexible, and scalable integrated photoelectrochemical cells, Adv. Energy Mater. **10**, 2002706 (2020).

[15] F. Fuchs, F. Caffy, R. Demadrille, T. Mélin, and B. Grévin, High-resolution Kelvin probe force microscopy imaging of interface dipoles and photogenerated charges in organic donor–acceptor photovoltaic blends, ACS Nano **10**, 739 (2016).

[16] J. Zhu, F. Fan, R. Chen, H. An, Z. Feng, and C. Li, Direct imaging of highly anisotropic photogenerated charge separations on different facets of a single $BiVO_4$ photocatalyst, Angew. Chem., Int. Ed. **54**, 9111 (2015).

[17] Z. Schumacher, Y. Miyahara, A. Spielhofer, and P. Grutter, Measurement of surface photovoltage by atomic force microscopy under pulsed illumination, Phys. Rev. Appl. **5**, 44018 (2016).

[18] Z. Schumacher, A. Spielhofer, Y. Miyahara, and P. Grutter, The limit of time resolution in frequency modulation atomic force microscopy by a pump-probe approach, Appl. Phys. Lett. **110**, 53111 (2017).

[19] L. Kronik and Y. Shapira, Surface photovoltage phenomena: Theory, experiment, and applications, Surf. Sci. Rep. **37**, 1 (1999).

[20] E. Escasain, E. Lopez-Elvira, A. M. Baro, J. Colchero, and E. Palacios-Lidon, Nanoscale surface photovoltage of organic semiconductors with two pass Kelvin probe microscopy, Nanotechnology **22**, 375704 (2011).

[21] Marti Checa, Addis S. Fuhr, Changhyo Sun, Rama Vasudevan, Maxim Ziatdinov, Ilia Ivanov, Seok Joon Yun, Kai Xiao, Alp Sehirlioglu, Yunseok Kim, Pankaj Sharma, Kyle P. Kelley, Neus Domingo, Stephen Jesse, and Liam Collins, High-speed mapping of surface charge dynamics using sparse scanning Kelvin probe force microscopy, Nat. Commun. **14**, 7196 (2023).

[22] R. Chen, F. Fan, and C. Li, Unraveling charge-separation mechanisms in photocatalyst particles by spatially resolved surface photovoltage techniques, Angew. Chem., Int. Ed. **61**, e202117567 (2022).

[23] L. R. Sheppard, T. Dittrich, and M. K. Nowotny, the impact of niobium surface segregation on charge separation in niobium-doped titanium dioxide, J. Phys. Chem. C **116**, 20923 (2012).

[24] J. Zheng, Y. Lyu, R. Wang, C. Xie, H. Zhou, S. P. Jiang, and S. Wang, Crystalline TiO_2 protective layer with graded oxygen defects for efficient and stable silicon-based photocathode, Nat. Commun. **9**, 1 (2018).

[25] Mohammad A. Alim, Tadeusz Bak, Armand J. Atanacio, Mihail Ionescu, Brendan Kennedy, William S. Price, Johan Du Plessis, Maryam Pourmahdavi, Meifang Zhou, Allan Torres, and Janusz Nowotny, Photocatalytic properties of Ta-doped TiO_2, Ionics **23**, 3517 (2017).

[26] S. Hu, M. R. Shaner, J. A. Beardslee, M. Lichterman, B. S. Brunschwig, and N. S. Lewis, Amorphous TiO_2 coatings stabilize Si, GaAs, and GaP photoanodes for efficient water oxidation, Science **344**, 1005 (2014).

[27] S. Hu, M. H. Richter, M. F. Lichterman, J. Beardslee, T. Mayer, B. S. Brunschwig, and N. S. Lewis, Electrical, photoelectrochemical, and photoelectron spectroscopic investigation of the interfacial transport and energetics of amorphous TiO_2/Si heterojunctions, J. Phys. Chem. C **120**, 3117 (2016).

[28] B. Seger, D. S. Tilley, T. Pedersen, P. C. K. Vesborg, O. Hansen, M. Grätzel, and I. Chorkendorff, Silicon protected with atomic layer deposited TiO_2: durability studies of photocathodic H_2 evolution, RSC Adv. **3**, 25902 (2013).

[29] S. Fengler, H. Kriegel, M. Schieda, H. Gutzmann, T. Klassen, M. Wollgarten, and T. Dittrich, Charge transfer in c-Si(n^{++})/TiO_2(ALD) at the amorphous/anatase transition: A transient surface photovoltage spectroscopy study, ACS Appl. Mater. Interfaces **12**, 3140 (2020).

[30] S. T. Nishanthi, S. Iyyapushpam, B. Sundarakannan, E. Subramanian, and D. Pathinettam Padiyan, Significance of crystallinity on the photoelectrochemical and photocatalytic activity of TiO_2 nanotube arrays, Appl. Surf. Sci. **313**, 449 (2014).

[31] J. Eichhorn, C. Kastl, J. K. Cooper, D. Ziegler, A. M. Schwartzberg, I. D. Sharp, and F. M. Toma, Nanoscale imaging of charge carrier transport in water splitting photoanodes, Nat. Commun. **9**, 2597 (2018).

[32] Janusz Nowotny, Mohammad Abdul Alim, Tadeusz Bak, Mohammad Asri Idris, Mihail Ionescu, Kathryn Prince, Mohd Zainizan Sahdan, Kamaruzzaman Sopian, Mohd Asri Mat Teridie, and Wolfgang Sigmund, Defect chemistry and defect engineering of TiO_2-based semiconductors for solar energy conversion, Chem. Soc. Rev. **44**, 8424 (2015).

[33] T. Dittrich and S. Fengler, *Surface Photovoltage Analysis of Photoactive Materials* (World Scientific, New Jersey London Singapore, 2020).

[34] A. Henning, G. Günzburger, R. Jöhr, Y. Rosenwaks, B. Bozic-Weber, C. E. Housecroft, E. C. Constable, E. Meyer, and T. Glatzel, Kelvin probe force microscopy of nanocrystalline TiO_2 photoelectrodes, Beilstein J. Nanotechnol. **4**, 418 (2013).

[35] P. Eaton and P. West, *Atomic Force Microscopy* (Oxford University Press, New York, 2010).

[36] R. Chen, F. Fan, T. Dittrich, and C. Li, Imaging photogenerated charge carriers on surfaces and interfaces of photocatalysts with surface photovoltage microscopy, Chem. Soc. Rev. **47**, 8238 (2018).

[37] M.-C. Wu, H.-C. Liao, Y.-C. Cho, G. Tóth, Y.-F. Chen, W.-F. Su, and K. Kordás, Photo-Kelvin probe force microscopy for photocatalytic performance characterization of single filament of TiO_2 nanofiber photocatalysts, J. Mater. Chem. A **1**, 5715 (2013).

[38] M.-C. Wu, *et al.*, Photocatalytic activity of nitrogen-doped TiO_2-based nanowires: A photo-assisted Kelvin probe force microscopy study, J. Nanopart. Res. **16**, 2143 (2013).

[39] T. Su, C. Yang, F. Niu, Y. Hua, Q. Xu, K. Hu, and L. Zhang, Spatial separation of photogenerated charges on the anisotropic facets of cuprous oxide, Inorg. Chem. Front. **10**, 3550 (2023).

[40] D. K. Schroder, Surface voltage and surface photovoltage: History, theory and applications, Meas. Sci. Technol. **12**, R16 (2001).

[41] C. Ros, T. Andreu, M. D. Hernández-Alonso, G. Penelas-Pérez, J. Arbiol, and J. R. Morante, Charge transfer characterization of ALD-grown TiO_2 protective layers in silicon photocathodes, ACS Appl. Mater. Interfaces **9**, 17932 (2017).

[42] B. Mei, T. Pedersen, P. Malacrida, D. Bae, R. Frydendal, O. Hansen, P. C. K. Vesborg, B. Seger, and I. Chorkendorff, Crystalline TiO_2: A generic and effective

electron-conducting protection layer for photoanodes and -cathodes, J. Phys. Chem. C **119**, 15019 (2015).

[43] M. K. Nowotny, P. Bogdanoff, T. Dittrich, S. Fiechter, A. Fujishima, and H. Tributsch, Observations of p-type semiconductivity in titanium dioxide at room temperature, Mater. Lett. **64**, 928 (2010).

[44] See Supplemental Material at http://link.aps.org/supplemental/10.1103/PRXEnergy.4.023010 for additional microsctructural characterization, as well further detailed analysis of the photovoltage transients, and a full description of the data analysis method, including analysis of KP data, and algorithms implemented for extraction of transients from a series of continuously acquired KPFM images.

[45] S. Sadewasser and T. Glatzel, *Kelvin Probe Force Microscopy: Measuring and Compensating Electrostatic Forces* (Springer, Heidelberg, 2011).

[46] L. Kou, Y. J. Li, T. Kamijyo, Y. Naitoh, and Y. Sugawara, Investigation of the surface potential of TiO_2 (110) by frequency-modulation Kelvin probe force microscopy, Nanotechnology **27**, 505704 (2016).

[47] N. Turetta, F. Sedona, A. Liscio, M. Sambi, and P. Samorì, Au(111) Surface Contamination in ambient conditions: Unravelling the dynamics of the work function in air, Adv. Mater. Interfaces **8**, 2100068 (2021).

[48] Christoph Kastl, Roland J. Koch, Christopher T. Chen, Johanna Eichhorn, Søren Ulstrup, Aaron Bostwick, Chris Jozwiak, Tevye R. Kuykendall, Nicholas J. Borys, Francesca M. Toma, Shaul Aloni, Alexander Weber-Bargioni, Eli Rotenberg, and Adam M. Schwartzberg, Effects of defects on band structure and excitons in WS_2 revealed by nanoscale photoemission spectroscopy, ACS Nano **13**, 1284 (2019).

[49] B. Zhao, Z. Gan, M. Johnson, E. Najafidehaghani, T. Rejek, A. George, R. H. Fink, A. Turchanin, and M. Halik, 2D van der Waals heterojunction of organic and inorganic monolayers for high responsivity phototransistors, Adv. Funct. Mater. **31**, 2105444 (2021).

[50] L. X. Chen and J. Yano, Deciphering photoinduced catalytic reaction mechanisms in natural and artificial photosynthetic systems on multiple temporal and spatial scales using X-ray probes, Chem. Rev. **124**, 5421 (2024).

[51] A. Litke, Y. Su, I. Tranca, T. Weber, E. J. M. Hensen, and J. P. Hofmann, Role of adsorbed water on charge carrier dynamics in photoexcited TiO_2, J. Phys. Chem. C **121**, 7514 (2017).

[52] Rosaria Verduci, Fabrizio Creazzo, Francesco Tavella, Salvatore Abate, Claudio Ampelli, Sandra Luber, Siglinda Perathoner, Giuseppe Cassone, Gabriele Centi, and Giovanna D'Angelo, Water structure in the first layers on TiO_2: A key factor for boosting solar-driven water-splitting performances, J. Am. Chem. Soc. **146**, 18061 (2024).

[53] https://doi.org/10.5281/zenodo.15235591